European Polymer Journal 138 (2020) 109954

Contents lists available at ScienceDirect

European Polymer Journal

journal homepage: www.elsevier.com/locate/europolj

Directly synthesized nitrogen-and-oxygen–doped microporous carbons derived from a bio-derived polybenzoxazine exhibiting high-performance supercapacitance and CO_2 uptake

Maha Mohamed Samy[a], Mohamed Gamal Mohamed[a,b], Shiao-Wei Kuo[a,c,*]

[a] Department of Materials and Optoelectronic Science, Center of Crystal Research, National Sun Yat-Sen University, Kaohsiung 804, Taiwan
[b] Chemistry Department, Faculty of Science, Assiut University, Assiut 71516, Egypt
[c] Department of Medicinal and Applied Chemistry, Kaohsiung Medical University, Kaohsiung 807, Taiwan

ARTICLE INFO

Keywords:
Benzoxazine
Ring-opening polymerization
KOH activation
Supercapacitor
CO_2 uptake

ABSTRACT

We have prepared a new bio-derived benzoxazine monomer (VFBZ-CN) through condensation of natural renewably sourced compounds—vanillin, formaldehyde, and furfurylamine—and then investigated its thermal stability and thermal curing polymerization behavior before and after polymerization at various temperatures. Differential scanning calorimetry revealed that VFBZ-CN possessed a thermal curing temperature (196 °C) lower than those of the typical Pa-type (263 °C) and Boz-Va benzoxazine (223.8 °C) monomers, presumably because the presence of its cyano groups facilitated ring opening of the oxazine units. We used various techniques to examine the porosity, morphology, structure, chemical composition, and electrochemical properties of the poly (VFBZ-CN) materials obtained after carbonization at 700 and 800 °C and KOH activation [giving poly(VFBZ-CN)-700 and poly(VFBZ-CN)-800, respectively]. The gravimetric capacitance of poly(VFBZ-CN)-800 (506 F g^{-1}) was higher than that of poly(VFBZ-CN)-700 (171 F g^{-1}) at 0.5 A g^{-1} in KOH solution; the former also displayed outstanding cycling stability, with retention of 99.43% of its capacitance after 2000 cycles. We attribute the superior performance of poly(VFBZ-CN)-800 as a supercapacitor electrode to its more porous carbon structure and higher N and oxygen atoms contents. In addition to their potential for energy storage, these N- and O-doped microporous carbons displayed high degrees of CO_2 capture.

1. Introduction

Supercapacitors are environmentally friendly materials that have attracted interest for their potential applications in electronic devices, electric vehicles, alternatives to batteries, and renewable power systems [1–6]. Based on their release mechanisms and modes of energy storage, there are two kinds of supercapacitors: pseudocapacitors and electrochemical double-layer capacitors (EDLCs) [7]. Several porous carbons materials having large specific surface area, high electrical conductivity, outstanding chemical stability, and good capacitive performance [e.g., graphene, carbon nanotubes, and activated carbons (ACs)] have been tested for their suitability in gas capture, electrochemical energy storage, and gas storage [3,8,9]. In particular, AC materials can function as energy storage when combined with EDLCs; their efficiency and performance depend on the structure and number of pores, with a large number of small carbon pores potentially accommodating a greater amount of solvated electrolyte ions. Nevertheless, this mechanism of operation of porous carbon materials generally decreases the energy density that can be achieved with AC-based supercapacitors [10]. Many recent studies have revealed that introducing nitrogen, oxygen, and phosphorus atoms into carbon materials can enhance the pseudocapacitance, due to the electron donating properties of these atoms [11,12]. Furthermore, these heteroatoms can induce reversible pseudocapacitance (by facilitating Faradaic electrochemical reactions at electrolyte–electrode interfaces) and enhance conductivity and surface wettability [13–17]. Thus, porous carbons containing heteroatoms—for example, nitrogen-doped hierarchical porous carbons (NHPCs)—are considered to be ideal electrode materials because of their combination of pseudocapacitance and double-layer capacitance [18], and also because they can be synthesized in a simple and scalable manner. Various carbon precursors have been converted into NHPCs (e.g., polyacrylonitrile, polyaniline, polythiophene, phenolic resin, biomass, and biomass derivatives) for use as novel materials for high-performance supercapacitors [19–22].

* Corresponding author at: Department of Materials and Optoelectronic Science, Center of Crystal Research, National Sun Yat-Sen University, Kaohsiung 804, Taiwan.
E-mail address: kuosw@faculty.nsysu.edu.tw (S.-W. Kuo).

https://doi.org/10.1016/j.eurpolymj.2020.109954
Received 10 July 2020; Received in revised form 5 August 2020; Accepted 11 August 2020
Available online 18 August 2020

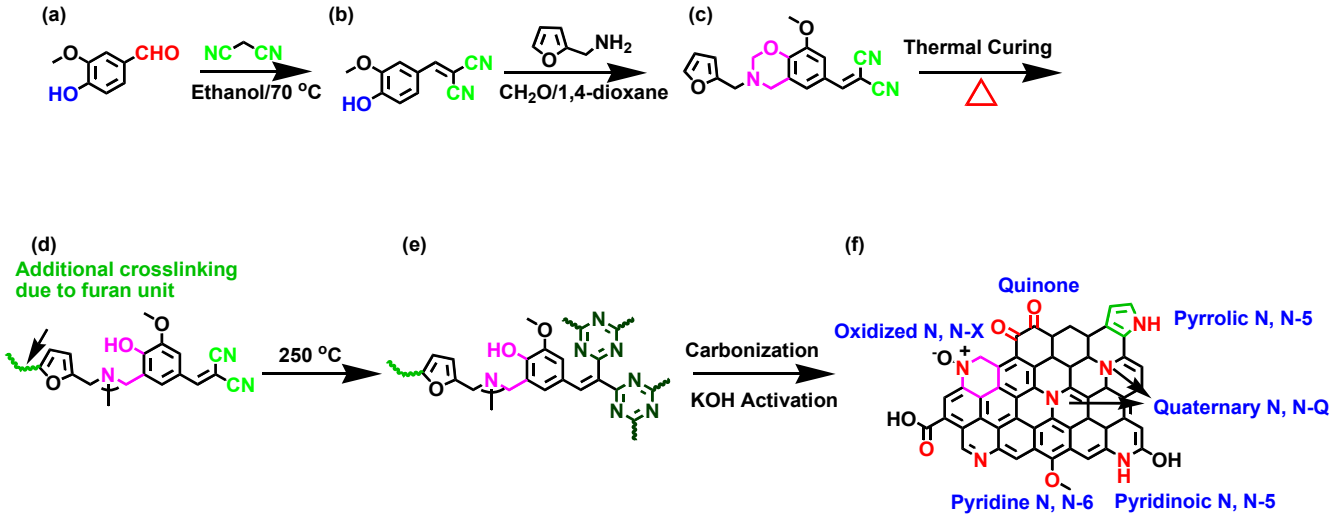

Scheme 1. Synthesis of (b) V-CN, (c) VFBZ-CN, (d) poly(VFBZ-CN), and (f) nitrogen-doped microporous carbons (NMCs).

Polybenzoxazines (PBZs) are novel thermosetting heterocyclic polymers obtained through thermal ring-opening polymerization (ROP) of benzoxazine (BZ) monomers [23], themselves prepared readily from phenols, paraformaldehyde [$(CH_2O)_n$], and amines through Mannich condensation [24–29]. PBZs are a promising class of high-performance NHPCs [30] because of their flexible molecular design, good chemical and electrical resistance, high char yields, good thermal stability, good flame retardancy, low surface free energies, and minimal shrinkage [31–36]. They also have a wide range of potential applications, including as adsorbents for CO_2, as cathodic material in batteries, in electronics, as coatings, and in the aerospace industry [37–43]. Moreover, their N atom content can be adjusted readily by merely changing the proportion or type of amine in the PBZ [44]. Nevertheless, we are aware of only a single previous report of supercapacitors prepared from NHPCs derived from PBZs. Wan *et al.* synthesized nitrogen-doped porous carbons (NPCs) from a nitrile-functionalized BZ through soft-templating and KOH activation; these materials featured an abundance of micro- and mesopores, high N and O atom contents, large surface areas, and good electrical conductivity [45].

In this study, we prepared a fully bio-derived monomer (VFBZ-CN) through the condensation of vanillin (V), furfurylamine (F), and $(CH_2O)_n$. Previous reports suggested that the incorporation of a furan ring into the BZ monomer would improve the thermal properties of the resulting PBZ [46]. In addition, the presence of cyano groups in the BZ structure would also increase the number of N atoms in the resulting microporous carbon skeletons after KOH activation, potentially enhancing the electronic conductivity and pore structure of the carbon materials. The synthesis of VFBZ-CN monomer was confirmed using nuclear magnetic resonance (NMR) and Fourier transform infrared (FTIR) spectroscopy. We used thermogravimetric analysis (TGA), differential scanning calorimetry (DSC), and FTIR spectroscopy to study the thermal stability and thermal ROP of the BZ monomer. Finally, we determined the electrochemical properties of the resulting NPC materials through cyclic voltammetry (CV).

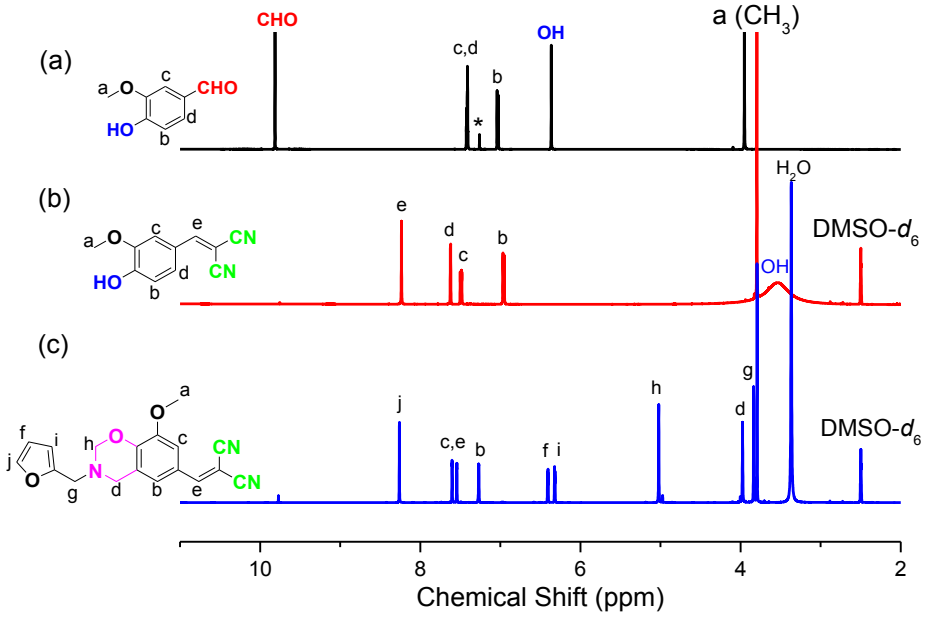

Fig. 1. ^{1}H NMR spectra of (a) vanillin, (b) V-CN, and (c) VFBZ-CN.

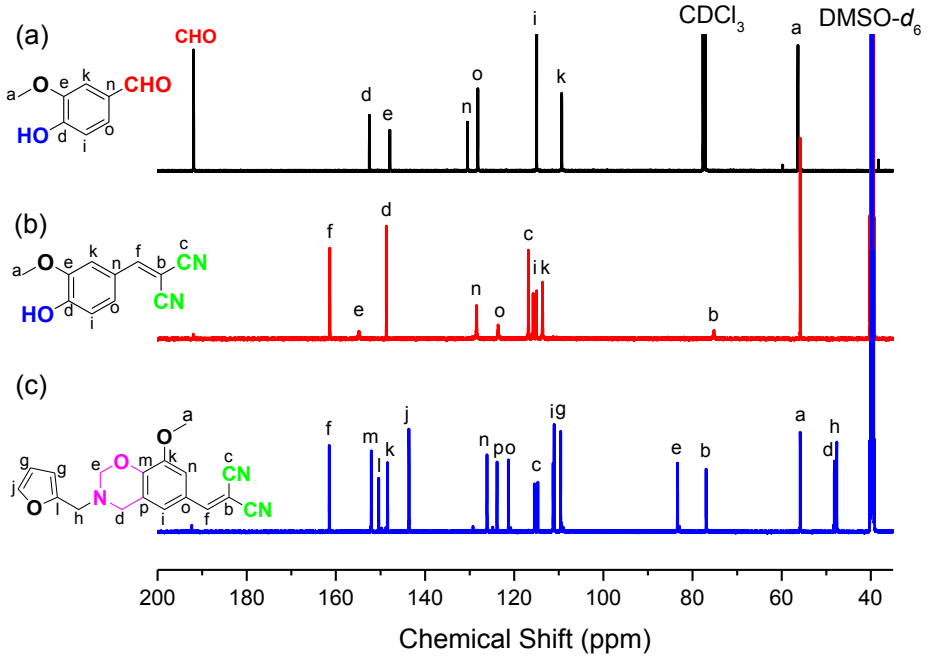

Fig. 2. ^{13}C NMR spectra of (a) vanillin, (b) V-CN, and (c) VFBZ-CN.

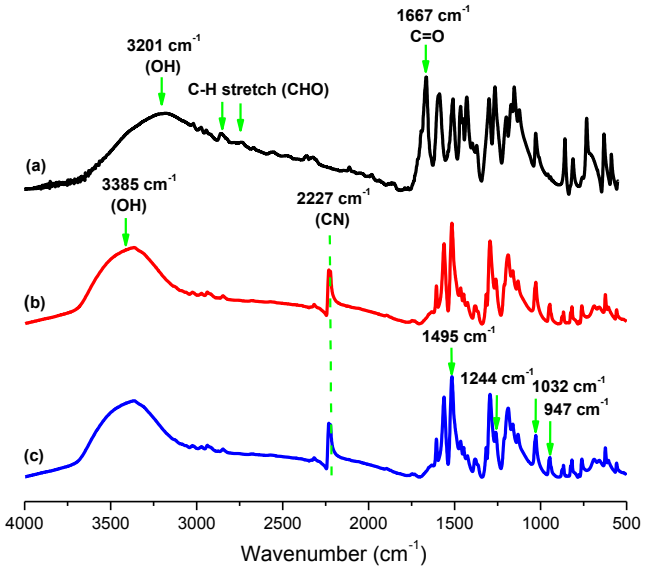

Fig. 3. FTIR spectra of (a) vanillin, (b) V-CN, and (c) VFBZ-CN.

2. Experimental

2.1. Materials

Vanillin, paraformaldehyde $(CH_2O)_n$, zinc acetate, malononitrile, sodium carbonate (Na_2CO_3), and furfurylamine were purchased from Acros. Dimethyl sulfoxide (DMSO), ethyl acetate (EA), hexane, 1,4-dioxane and absolute ethanol (EtOH) were purchased from Alfa Aesar.

2.2. 2-(4-Hydroxy-3-methoxybenzylidene)malononitrile (V-CN)

Vanillin (15.2 g, 100 mmol), malononitrile (6.60 g, 100 mmol), and zinc acetate (0.20 g, 2.40 mmol) were stirred in absolute EtOH (50 mL) at 80 °C for 8 h. The solvent was evaporated and then the residue was washed with hexane to afford a yellow powder (yield: 64%). FTIR (KBr, cm^{-1}): 3385 (OH), 2227 (CN); ^{1}H NMR (DMSO-d_6, δ, ppm): 3.81 (s, 3H), 6.98 (s, 1H), 7.51 (s, 1H), 7.65 (s, 1H), 8.29 (s, 1H), 10.81 (s 1H); ^{13}C NMR (DMSO-d_6, δ, ppm): 56.11, 76.42, 113.68, 115.65, 115.86, 116.86, 122.84, 128.14, 147.92 155.16, 163.57.

2.3. 2-((3-(Fur-2-ylmethyl)-8-methoxy-3,4-dihydro-2H-benzo[e][1,3] oxazine 6yl)methylene)malononitrile (VFBZ-CN)

A solution of V-CN (0.50 g, 2.0 mmol), furfurylamine (0.24 g, 2.0 mmol), and $(CH_2O)_n$ (0.16 g, 5.0 mmol) in 1,4-dioxane (50 mL) was heated at 110 °C under N_2 for 24 h. The solvent was evaporated through vacuum distillation to afford a brown residue, which was purified through column chromatography (SiO_2; hexane/EtOAc, 1:1) to give a yellow solid (yield: 60%). FTIR (KBr, cm^{-1}): 2227 (CN), 1244 (Ar—O—C), 947 (oxazine); ^{1}H NMR (DMSO-d_6, δ, ppm): 3.83 (s, 2H, furyl–CH_2N), 3.79 (s, 1H, CH_3), 3.99 (s, 2H, ArCH_2N), 5.03 (s, 2H, OCH_2N), 6.32–7.61 (m, CH aromatic), 8.27 (s, 1H, CH=CCNCN); ^{13}C NMR (DMSO-d_6, δ, ppm): 47.40, 47.94, 55.54, 82.47, 76.54, 82.93, 109.01, 110.47, 110.70, 114.10, 114.89, 120.68, 123.22, 125.45, 142.87, 147.63, 149.67, 151.27, 160.65.

2.4. Poly(VFBZ-CN)

The BZ monomer VFBZ-CN was cured thermally at (110, 150, 180, 210, and 250 °C for 2 h at each temperature) to give a dark-brown solid.

2.5. Poly(VFBZ-CN)-700 and Poly(VFBZ-CN)-800

VFBZ-CN (1.00 g) was cured thermally at 250 °C for 4 h. The resulting PBZ sample was calcinated in a furnace (heating rate: 5 °C min^{-1}) up to a temperature of 600 °C for 3 h. KOH solution [the weight ratio of KOH/poly(VFBZ-CN) = 1/1] was added to the calcinated sample and then the mixture was stirred at 25 °C for 24 h. The water was evaporated under vacuum at 120 °C for 24 h. Finally, the sample was activated at either 700 or 800 °C for 8 h in a tubular furnace (heating rate: 5 °C min^{-1}) under a N_2 atmosphere. After cooling to room temperature, the product was washed with deionized water and acetone, then the black solid was dried at 100 °C for 48 h.

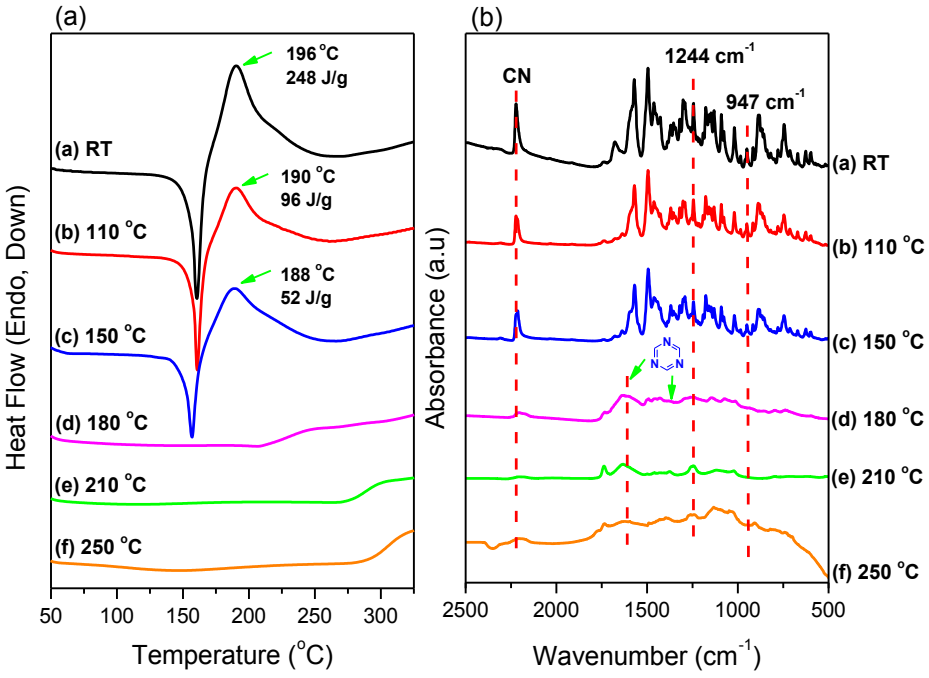

Fig. 4. (a) Dynamic DSC exothermic curves and (b) FTIR spectra for VFBZ-CN, recorded after each curing stage.

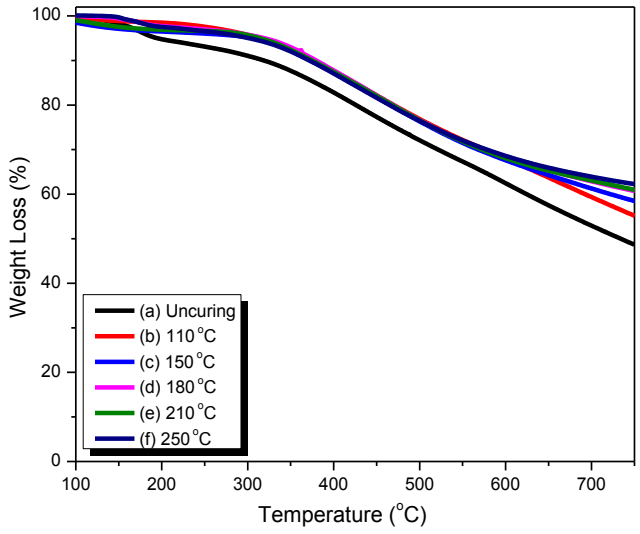

Fig. 5. TGA analyses of VFBZ-CN, recorded after each curing stage.

3. Results and discussion

3.1. Synthesis of V-CN and VFBZ-CN

Scheme 1 presents our synthetic route toward V-CN and VFBZ-CN. First, we prepared V-CN through the reaction of vanillin with malononitrile in the presence zinc acetate in absolute EtOH. Then, we subjected V-CN to Mannich condensation with $(CH_2O)_n$ and furfurylamine 1,4-dioxane at 110 °C to obtain VFBZ-CN.

The chemical structures of vanillin, V-CN, and VFBZ-CN were confirmed through NMR and FTIR spectroscopy. The ^{1}H NMR spectrum of vanillin [Fig. 1(a)] features signals at 3.93, 6.34, 7.03–7.45, and 9.82 ppm representing the protons of its CH_3, OH, aromatic, and CHO units, respectively. In the ^{1}H NMR spectrum of V-CN [Fig. 1(b)], a sharp singlet appears at 8.23 ppm, corresponding to the CH═C$(CN)_2$ unit, but no signal is present for an aldehydic group, confirming the completeness of the Knoevenagel reaction. The presence of the oxazine ring in VFBZ-CN was confirmed by the appearance [Fig. 1(c)] of two signals at 3.99 and 5.03 ppm for the $ArCH_2N$ and OCH_2N moieties, respectively. In addition, this ^{1}H NMR spectrum of VFBZ-CN exhibited a signal at 3.83 ppm for the furyl–CH_2N (g) unit and three signals at 6.32, 6.42, and 8.25 ppm representing the furyl moiety.

The ^{13}C NMR spectrum of vanillin [Fig. 2(a)] features characteristic signals at 56.38, 109.32–152.48, and 192.11 ppm, representing the carbon nuclei of the CH_3, aromatic, and CHO units, respectively. In the ^{13}C NMR spectrum of V-CN [Fig. 2(b)] three new signals appeared, at 75.30, 117.00, and 161.65 ppm, corresponding to the carbon nuclei of the CH═C(CN)$_2$ (f), CN (c), and CH═C$(CN)_2$ (b) moieties, respectively. Fig. 2(c) reveals signals at 48.10 and 83.30 ppm, representing the $ArCH_2N$ and OCH_2N units, respectively, of the oxazine ring, in the ^{13}C NMR spectrum of VFBZ-CN. In addition, signals of the carbon nuclei of the furan ring appeared at 109.61, 110.78, and 143.77 ppm.

The FTIR spectrum of vanillin [Fig. 3(a)] is characterized by absorption bands at 3201 cm^{-1} for the phenolic OH group, 2852 and 2750 cm^{-1} for the C–H bond of the aldehydic group, and 1667 cm^{-1} for the C═O bond. The FTIR spectrum of V-CN featured no absorption band for the C═O bond and exhibited a new sharp peak at 2227 cm^{-1} for the cyano group [Fig. 3(b)]. The FTIR spectrum of VFBZ-CN [Fig. 3(c)] displayed new absorption bands for the BZ moiety at 947, 1495, 1244, and 1032 cm^{-1}, representing out-of-plane C–H bending, trisubstituted benzene ring, asymmetric C–O–C stretching, and symmetric C–O–C stretching, respectively. In addition, the absence of any absorption bands for the phenolic OH group of vanillin and the NH_2 group of furfurylamine, and the presence of a band at 2237 cm^{-1} for the CN moiety and the absorption bands at 1563 and 760 cm^{-1} for the furan group, confirmed the synthesis of this new VFBZ-CN monomer in high purity.

3.2. Thermal curing polymerization of the VFBZ-CN monomer

The DSC profile of the uncured VFBZ-CN [Fig. 4(a)] revealed a sharp melting point at 160 °C, confirming the high purity of this monomer, followed by ROP at 196 °C with a reaction heat of 248 J g^{-1}. Thus, the monomer VFBZ-CN possesses an exothermic curing temperature lower than those of the typical Pa-type monomer 3-phenyl-3,4-dihydro-2*H*-benzoxazine (263 °C) [47,48], the monomer Boz-Va

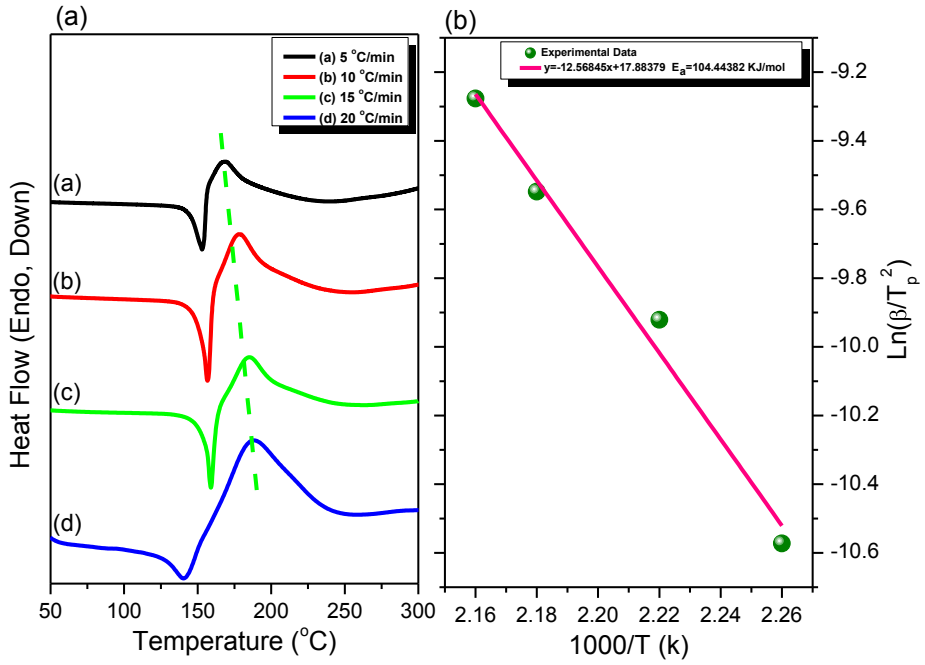

Fig. 6. (a) Dynamic DSC exothermic curve of VFBZ-CN, recorded at various heating rates. (b) Kissinger plots for determination of the values of E_a of VFBZ-CN.

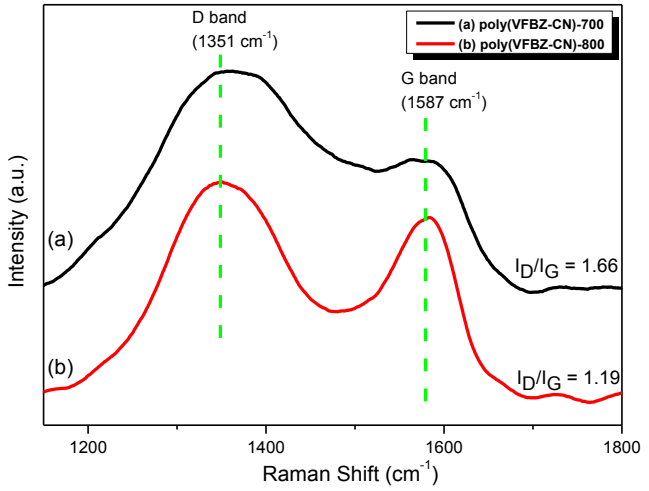

Fig. 7. Raman spectra of (a) poly(VFBZ-CN)-700 and (b) poly(VFBZ-CN)-800.

(223.8 °C) [49], the monomer *p*HMTI-*pan* (287.5 °C) [50] and the monomer *o*HPNI-*man* (287.5 °C) [51] due to the basicity and catalytic effect of the cyano groups. The curing polymerization temperature and polymerization enthalpy of VFBZ-CN both decreased after thermal treatment at 110 °C (190 °C and 96 J g^{-1}, respectively) and 150 °C (188 °C and 52 J g^{-1}, respectively). Furthermore, the exothermic curing temperature and the heat of reaction disappeared after increasing the thermal treatment temperature from 180 to 250 °C, consistent with full thermal curing of the monomer VFBZ-CN and formation of poly(VFBZ-CN). In addition, we recorded FTIR spectra to examine the thermal curing behavior of VFBZ-CN at these various temperatures. Fig. 4(b) reveals that the absorption bands of the BZ ring at 947, 1244, and 1032 cm^{-1} decreased after curing at 180 and 210 °C and disappeared completely at 250 °C, consistent with the DSC data. Furthermore, upon increasing the curing temperature from 180 to 250 °C, the intensity of the absorption band of the reactive cyano group of VFBZ-CN at 2235 cm^{-1} decreased and new absorption peaks appeared centered at 1385 and 1632 cm^{-1}, indicating that the reactive cyano groups in poly(VFBZ-CN) had transformed completely into triazine rings and that an extra extended two-dimensional (2D) framework had formed, presumably improving the crosslinking density and thermal stability of the poly(VFBZ-CN) [44,45,52].

We used the temperature for 10% weight loss (T_{d10}) and the char yield to characterize the thermal stability of the monomer VFBZ-CN before and after each curing stage (Fig. 5). From the TGA analysis, the uncured VFBZ-CN monomer exhibited a thermal decomposition temperature and char yield of 319 °C and 45 wt%, respectively. After its thermal treatment at 110, 150, 180, 210, and 250 °C, the values of T_{d10} were 373, 377, 380, 378, and 379 °C, respectively, and the char yields were 52, 57, 59, 59.40 and 62 wt%, respectively. The char yield of poly(VFBZ-CN) after calcining at 250 °C (62 wt%) was remarkable when compared with those of the Pa-type BZ and poly(Boz-Va), which displayed char yields of 48 and 60 wt%, respectively, after thermal curing at only 250 °C. This superior stability was presumably due to the crosslinking networks of poly(VFBZ-CN), additional crosslinking from the furan unit and the extended 2D framework arising from its triazine rings [53,54].

We recorded the DSC profiles of poly(VFBZ-CN) at various heating rates (5, 10, 15, and 20 °C min^{-1}) [Fig. 6(a)]. The curing temperature increased upon increasing the heating rate from 5 to 20 °C min^{-1}. We determined the activation energy of the reaction using the Kissinger method [55], calculated from Eq. (1):

$$\ln\left(\frac{\beta}{T_p^2}\right) = \ln\left(\frac{AR}{E_a}\right) - \frac{E_a}{RT} \quad (1)$$

where β is the heating rate, R is the gas constant, A is the pre-exponential factor, and T_P is the exothermic curing peak. According to the Kissinger method, we plotted $\ln(\beta/T_P^2)$ with respect to $1/T_P^2$ to get the value of E_a from the slope of the line [Fig. 6(b)]. The activation energy for VFBZ-CN (104 kJ mol^{-1}) was lower than that for 7-(furylmethyl)-7,8-dihydro-6*H*-[1,3]dioxolobenzoxazine (S-fa, 113.6 kJ mol^{-1}) [56], suggesting that the cyano groups in the monomer VFBZ-CN catalyzed the ROP at lower temperature.

3.3. Structural characterization of poly(VFBZ-CN)-700 and poly(VFBZ-CN)-800

We used X-ray diffraction (XRD) and Raman spectroscopy to investigate the graphitic structures of our carbon materials poly(VFBZ-

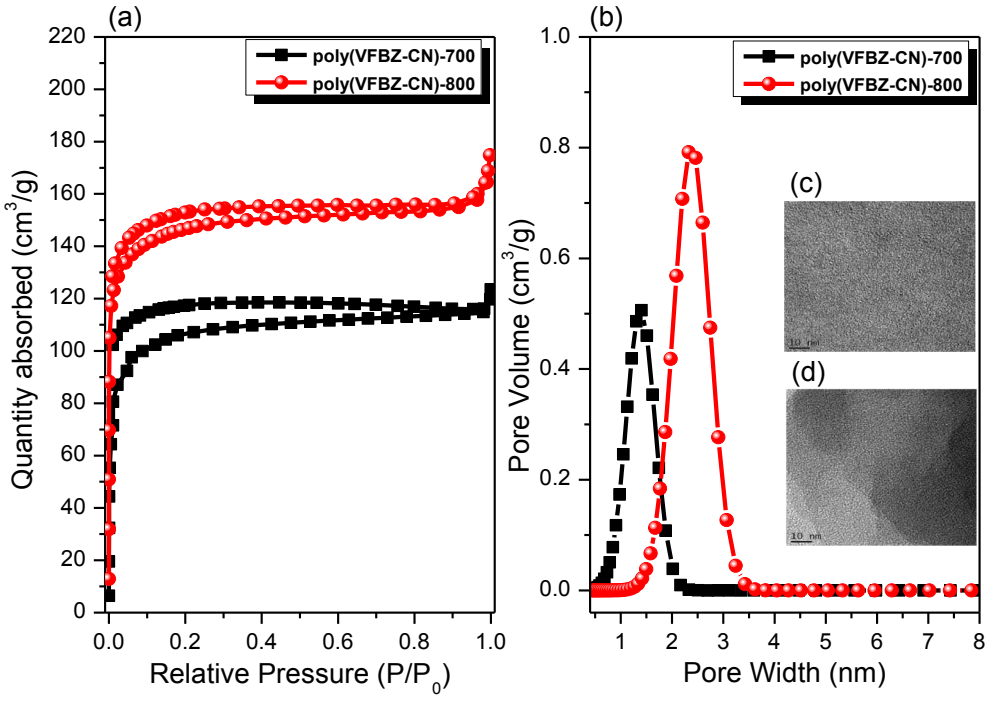

Fig. 8. (a) N_2 adsorption/desorption isotherms, (b) pore size distributions, and (c, d) TEM images of poly(VFBZ-CN)-700 and poly(VFBZ-CN)-800.

Table 1
Thermal properties, XPS data, surface areas, and electrochemical performance of the BZ samples.

Samples	T_{d10} (°C)	Char yield (wt%)	XPS analysis (%)			S_{micro} ($m^2\ g^{-1}$)	Specific capacitance ($F\ g^{-1}$)
			C	O	N		
VFBZ-CN	319	45.15	–	–	–	–	–
poly(VFBZ-CN)	379	62	–	–	–	–	–
poly(VFBZ-CN)-700	723	87	44.71	51.48	2.33	408	171
poly(VFBZ-CN)-800	734	87	61.66	36.01	3.81	560	506

CN)-700 and poly(VFBZ-CN)-800. The XRD profiles of poly(VFBZ-CN)-700 and poly(VFBZ-CN)-800 (Fig. S1) both featured diffraction peaks centered at values of 2θ of 12 and 25°, corresponding to their 002 and 100 planes, respectively, as well as peaks at a value of 2θ of 44°, representing graphitic carbon [53]. Thus, the XRD patterns suggested that poly(VFBZ-CN)-700 and poly(VFBZ-CN)-800 both possessed the characteristics of amorphous porous carbons. Fig. 7 displays the Raman spectra of the NPC materials we obtained after KOH activation of poly (VFBZ-CN)-700 and poly(VFBZ-CN)-800. D and G-bands appeared at 1359 and 1584 cm^{-1} for poly(VFBZ-CN)-700, respectively; and 1352 and 1582 cm^{-1} for poly(VFBZ-CN)-800. The position of the G-band for poly(VFBZ-CN)-800 was closer to that of graphene (1581 cm^{-1}) indicating that poly(VFBZ-CN)-800 provided had a better graphenoid structure than poly(VFBZ-CN)-700. The integral ratios of the D- and G-bands (I_D/I_G), characterizing the graphitic degrees of poly(VFBZ-CN)-700 and poly(VFBZ-CN)-800, were 1.66 and 1.19, respectively, indicating that poly(VFBZ-CN)-800 was more highly graphitized (i.e., it was a more regular carbon material and had a less disordered structure) than poly(VFBZ-CN)-700 [57,58].

We used N_2 adsorption/desorption to investigate the porosities of poly(VFBZ-CN)-700 and poly(VFBZ-CN)-800 (Fig. 8, Table 1). The isothermal curves of poly(VFBZ-CN)-700 and poly(VFBZ-CN)-800 [Fig. 8(a)] revealed rapidly increasing N_2 absorption in the low pressure regime ($P/P_0 < 0.10$), slight increases in the moderate pressure range ($P/P_0 = 0.1–0.9$), and finally sharp increases in the high pressure regime ($P/P_0 = 0.9–1$), suggesting the presence of micropores in our N-doped carbon materials (i.e., type-I isotherms). Moreover, the specific surface area of poly(VFBZ-CN)-800 (560 $m^2\ g^{-1}$) was higher than that of poly(VFBZ-CN)-700 (408 $m^2\ g^{-1}$), suggesting the formation of an ultramicroporous structure after KOH activation of poly(VFBZ-CN)-800 (i.e., increased BET surface area, micropore volume, and micropore pore size after carbonization and activation by KOH) [53,54]. Pore size distribution curves [Fig. 8(b)] revealed that the average pore size and total pore volume were 1.42 nm and 0.80 $cm^3\ g^{-1}$, respectively, for poly(VFBZ-CN)-700 and 2.37 nm and 1.254 $cm^3\ g^{-1}$, respectively, for poly(VFBZ-CN)-800, making them microporous or even mesoporous materials. Transmission electron microscopy [TEM; Fig. 8(c) and (d)] and scanning electron microscopy [SEM; Fig. S2(a) and S2(b)] images confirmed that poly(VFBZ-CN)-700 and poly(VFBZ-CN)-800 had porous structures.

From the TGA analysis [Fig. S3], both poly(VFBZ-CN)-700 and poly (VFBZ-CN)-800 displayed higher char yield (87 wt%) than that of poly (VFBZ-CN) (62 wt%), indicating that our materials possessed outstanding thermal stability. The surface wettability and conductivity of carbon materials are typically enhanced by the presence of heteroatoms [e.g., N and O atoms], which promote their capacity as supercapacitors [59]. We used X-ray photoelectron spectroscopy (XPS) to identify the chemical compositions of the microporous carbon materials poly(VFBZ-CN)-700 and poly(VFBZ-CN)-800 and the percentages of C, N, and O atoms on their surfaces. The XPS profiles featured peaks at 286, 532, and 690 eV representing the C, N, and O atoms on the surfaces of poly (VFBZ-CN)-700 and poly(VFBZ-CN)-800 (Fig. S4). To investigate the degrees of graphitization of our poly(VFBZ-CN) materials calcined at 700 and 800 °C, we fitted the peaks for their N 1 s and O 1 s binding

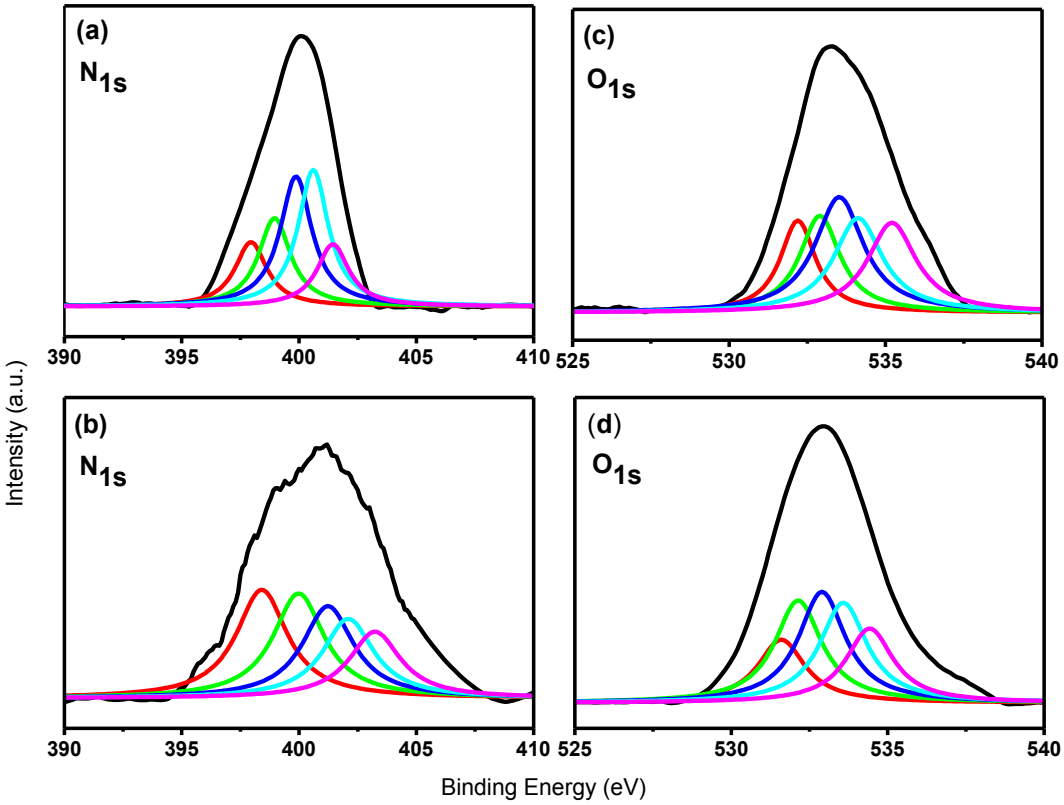

Fig. 9. XPS spectra (N 1 s and O 1 s orbitals) of (a, c) poly(VFBZ-CN)-700 and (b, d) poly(VFBZ-CN)-800.

Table 2
Area fractions determined from the N 1s and O 1s XPS spectra of the microporous carbons poly(VFBZ-CN)-700 and poly(VFBZ-CN)-800.

Samples	N species				O species				
	N-6	N-5	N-Q	N-X	Quinone	C═O	C—O	C—OH	H_2O
poly(VFBZ-CN)-700	27.32	27.48	13.50	13.07	15.12	18.11	25.74	21.14	20.09
poly(VFBZ-CN)-800	23.32	24.05	20.43	14.64	10.29	13.15	38.06	24.21	14.29

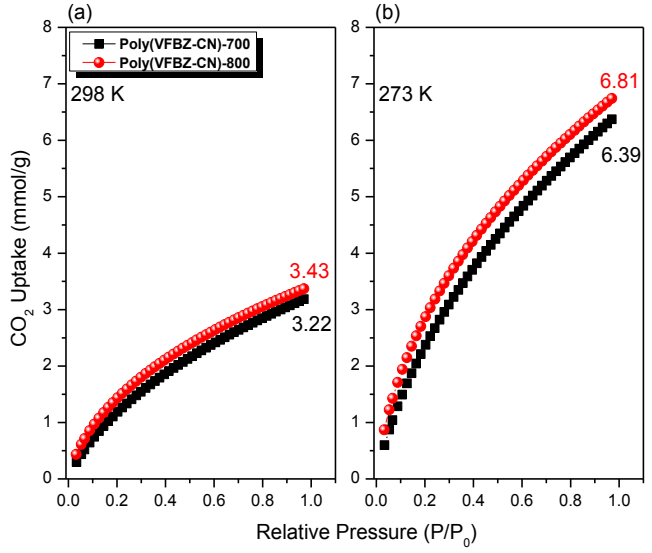

Fig. 10. CO_2 adsorption of poly(VFBZ-CN)-700 and poly(VFBZ-CN)-800 at (a) 298 and (b) 273 K.

energies on their surfaces [Fig. 9, Table 2]. Four types of N atom species were present on the surfaces of the microporous materials poly(VFBZ-CN)-700 and poly(VFBZ-CN)-800 [Fig. 9(a) and (b)]: pyridinic N atoms (ca. 398 eV), quaternary N atoms (ca. 401 eV), oxidized N atoms (ca. 403 eV), and pyridonic N atoms (ca. 400 eV) [60]. Furthermore, Fig. 9(c) and (d) reveal signals for five types of O species near 531, 532, 533, 534, and 535 eV, representing quinone species, C═O units, C—O units, C—OH units, and adsorbed H_2O [61]. The N atom contents on the surfaces of poly(VFBZ-CN)-700 and poly(VFBZ-CN)-800 were 2.33 and 3.81 wt%, respectively, while their O atom contents were 36.01 and 51.48 wt%, respectively (Table 2) [62]. The contents of N-6 and N-5 species in our poly(VFBZ-CN)-700 and poly(VFBZ-CN)-800 microporous carbon materials were higher than those of other N-doped carbon materials [62–64].

Therefore, we suspected that our new NPC materials would exhibit high electrochemical performance and be useful for CO_2 capture. From CO_2 uptake measurements [Fig. 10(a) and (b)], the degrees of CO_2 capture by poly(VFBZ-CN)-700 and poly(VFBZ-CN)-800 at 298 K were 3.22 and 3.43 mmol g^{-1}, respectively, while at 273 K they were 6.39 and 6.81 mmol g^{-1}, respectively. The superior CO_2 capture performance of poly(VFBZ-CN)-800 was due presumably to its higher N atom content (3.81%) and Brunauer–Emmett–Teller (BET) surface area (560 m^2 g^{-1}) and larger total volume (1.254 cm^3 g^{-1}) and average pore size (2.37 nm), relative to those of poly(VFBZ-CN)-700. Table S1

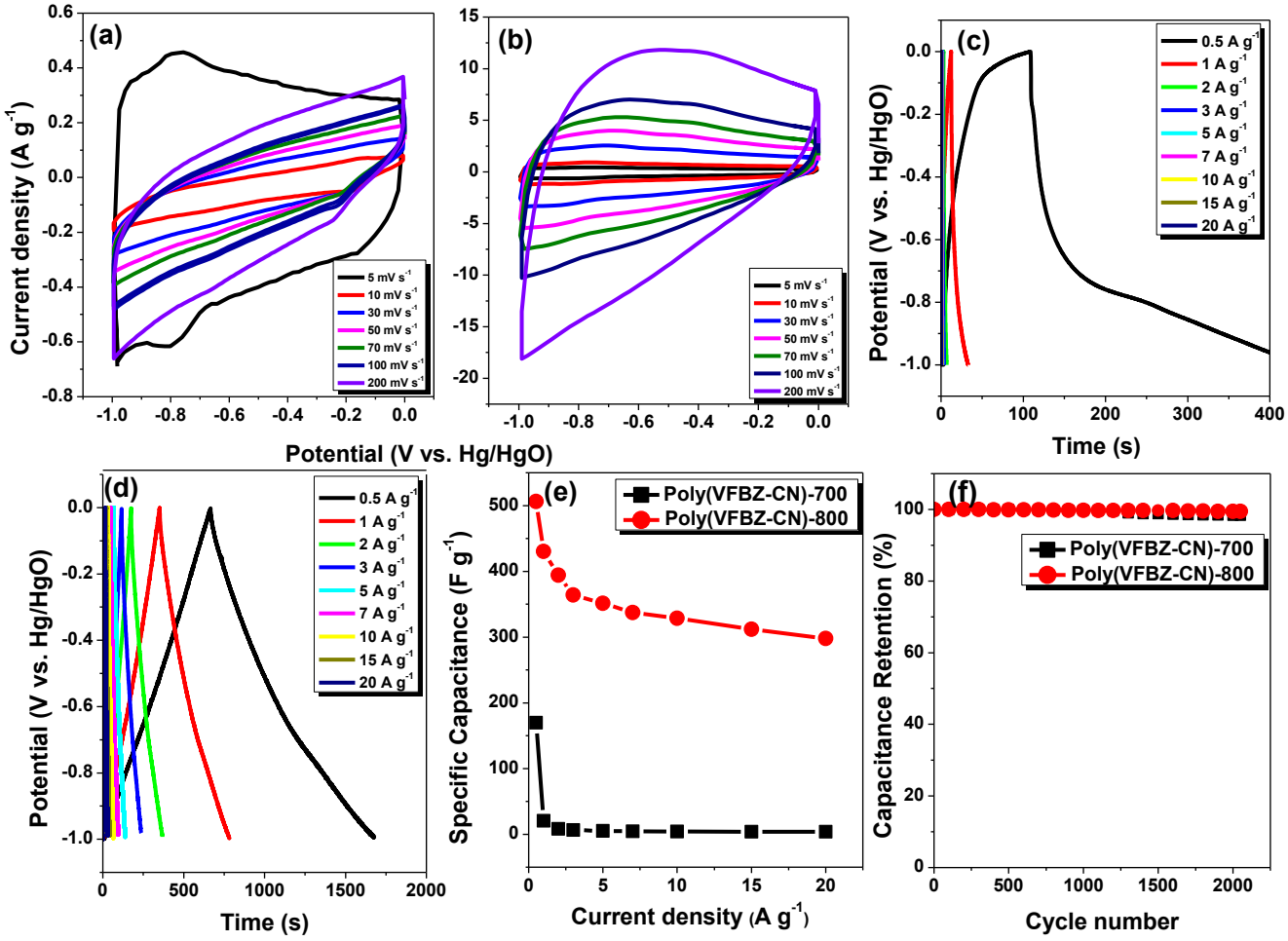

Fig. 11. (a, b) CV curves of (a) poly(VFBZ-CN)-700 and (b) poly(VFBZ-CN)-800. (c, d) GCD curves of (c) poly(VFBZ-CN)-700 and (d) poly(VFBZ-CN)-800, recorded at various currents. (e) Specific capacitances of poly(VFBZ-CN)-700 and poly(VFBZ-CN)-800, recorded at current densities from 0.5 to 20 A g^{-1}. (f) Cycling stabilities of poly(VFBZ-CN)-700 and poly(VFBZ-CN)-800 electrodes, recorded at a current density of 10 A g^{-1} over 2000 cycles.

shows the performance data of poly(VFBZ-CN)-700 and poly(VFBZ-CN)-800 compared with those of other previously reported N-containing porous carbon materials derived from PBZ matrices.

3.4. Electrochemical performance

We used CV to measure the electrochemical properties of our poly (VFBZ-CN) microporous carbon materials in 1 M aqueous KOH as the electrolyte [Fig. 11(a) and (b)]. The CV curves of poly(VFBZ-CN)-700 and poly(VFBZ-CN)-800 were both rectangle-like shapes featuring humps—typical characteristics of electric double-layer capacitance and pseudocapacitance [65–69]. Fig. 11(c) and (d) display the galvanostatic charge/discharge (GCD) curves of poly(VFBZ-CN)-700 and poly(VFBZ-CN)-800 recorded at current densities in the range 0.5–20 A g^{-1}. The shape of each GCD curve for the two microporous carbon materials was triangular, suggesting the coexistence of electric double-layer capacitance and pseudocapacitance, resulting from the presence of graphitic microporous carbon structures featuring various kinds of functionalized units (pyridinic and pyrrolic N atoms; C=O and phenolic OH groups [70–74]. We used equation (S1) to determine the specific capacitances poly(VFBZ-CN)-800 and poly(VFBZ-CN)-700 from the GCD curves (Fig. 11(e)). Fig. 11(e) reveals that the capacitance of the two poly (VFBZ-CN) electrodes decreased slightly upon increasing the current density from 1 to 20 A g^{-1}, revealing their rapid charge/discharge characteristics. Notably, at a current density of 0.5 A g^{-1}, the capacitance of the poly(VFBZ-CN)-800 electrode (506 F g^{-1}) was higher than that of the poly(VFBZ-CN)-700 electrode (171 F g^{-1}), presumably because the former's microporosity, graphitic structure, and higher content of accessible surface O atoms (36.01 wt%) led to a larger pseudocapacitance. To investigate the cycling stability of the poly(VFBZ-CN)-700 and poly(VFBZ-CN)-800 electrodes, we performed GCD studies at a current density of 10 A g^{-1}. After 2000 cycles in the KOH electrolyte, the rates of capacitance retention were 98.33 and 99.43% for the poly(VFBZ-CN)-700 and poly(VFBZ-CN)-800 electrodes, respectively [Fig. 11(f)], indicative of outstanding long-term cycling stability. Xu *et al.* synthesized NCMs from aniline-phenol BZ (NCM-700, NCM-800, NCM-900) and aniline-cardanol BZ (ACNCM-900) at various carbonization temperatures. Comparing the specific capacitances of NCM-700, NCM-800, NCM-900, and ACNCM-900 at various current densities (0.25–5.0 A g^{-1}), they found that NCM-900 had the highest electrochemical specific capacitance (reaching a high of 460F g^{-1}) at all current densities. Also, after 2000 cycles, the capacitance retention of NCM-900 was 96.1%, presumably because of its high BET surface area (798 m^2 g^{-1}) and large content of N atoms (4.95%) [75]. Furthermore, Liu *et al.* prepared the N- and O-containing carbon compounds NOPC-x and NOPC-bis-CN-x from a bio-based BZ. At 1 A g^{-1}, the electrochemical performance of NOPC-bis-CN-3 (167.3 F g^{-1}) was superior to that of NOPC-x, with greater than 80% of retention capability at 10 A g^{-1} [46]. In addition, Wan *et al.* prepared the NHPC materials NPC-600, HPC-600, and HPC-700 from a nitrile-functionalized BZ and obtained specific capacitances of 254.4, 375.4, and 279.7 F g^{-1}, respectively, at 1 A g^{-1} [44]. Interestingly, the specific capacitances of our

poly(VFBZ-CN)-800 electrode are higher relative to those of all of these previously reported NPC materials derived from PBZ matrices (Table S2), presumably because our material was a porous carbon having a higher degree of graphitization, larger pores, and greater N and O atom contents (based on XPS, Raman spectral, and BET analyses). Thus, poly (VFBZ-CN)-800 has excellent potential for application in high-rate supercapacitors.

4. Conclusions

We have synthesized a new bio-based BZ monomer (VFBZ-CN) from the natural materials vanillin, furfurylamine, and $(CH_2O)_n$. VFBZ-CN possesses a lower thermal curing temperature (196 °C) and excellent thermal stability after thermal curing at 250 °C, when compared with typical BZ monomers, as determined through DSC and TGA analyses. Furthermore, at 0.5 A g^{-1}, an electrode prepared from poly(VFBZ-CN)-800 featured a specific capacitance (506 F g^{-1}) larger than that of the electrode prepared from poly(VFBZ-CN)-700 (171 F g^{-1}). Moreover, the poly(VFBZ-CN)-800 electrode was highly stable, with a capacitance ratio of 99.43% at a current density of 10 A g^{-1} after 2000 charge/discharge cycles. In addition to use in a supercapacitor, our poly(VFBZ-CN)-800 microporous carbon material derived from renewable resources has great potential for application in CO_2 capture.

CRediT authorship contribution statement

Maha Mohamed Samy: Investigation, Formal analysis. **Mohamed Gamal Mohamed:** Investigation, Formal analysis, Writing - original draft, Writing - review & editing. **Shiao-Wei Kuo:** Supervision, Writing - original draft, Writing - review & editing.

Declaration of Competing Interest

The authors declare that they have no known competing financial interests or personal relationships that could have appeared to influence the work reported in this paper.

Acknowledgments

This study was supported financially by the Ministry of Science and Technology, Taiwan, under contracts MOST 108–2638-E-002–003-MY2, 106–2221-E-110–067-MY3, 108–2221-E-110–014-MY3, and 108–2218-E-110–013-MY3.

Appendix A. Supplementary material

Supplementary data to this article can be found online at https://doi.org/10.1016/j.eurpolymj.2020.109954.

References

[1] J. Miller, P. Simon, Electrochemical capacitors for energy management, Science 321 (2008) 651–652.
[2] A. Vlad, N. Singh, C. Galande, P. Ajayan, Design considerations for unconventional electrochemical energy storage architectures, Adv. Energy Mater. 5 (2015) 1402115.
[3] L.L. Zhang, X.S. Zhao, Carbon-based materials as supercapacitor electrodes, Chem. Soc. Rev. 38 (2009) 2520–2531.
[4] C. Liu, Z. Yu, D. Neff, A. Zhamu, B.Z. Jang, Graphene-based supercapacitor with an ultrahigh energy density, Nano Lett. 10 (2010) 4863–4868.
[5] Y. Wang, Z.Q. Shi, Y. Huang, Y.F. Ma, C.Y. Wang, M.M. Chen, Y.S. Chen, Supercapacitor devices based on grapheme materials, J. Phys. Chem. C 113 (2009) 13103–13107.
[6] Y.W. Zhu, S. Murali, M.D. Stoller, K.J. Ganesh, W.W. Cai, P.J. Ferreira, A. Pirkle, R.M. Wallace, K.A. Cychosz, M. Thommes, D. Su, E.A. Stach, R.S. Ruoff, Carbon-based supercapacitors produced by activation of graphene, Science 332 (2011) 1537–1541.
[7] H.F. An, Y. Wang, X.Y. Wang, N. Li, L.P. Zheng, The preparation of PANI/CA composite electrode material for supercapacitors and its electrochemical performance, J. Solid State Electrochem. 14 (2010) 651–657.
[8] L. Zhang, R. Zhou, X. Zhao, Graphene-based materials as supercapacitor electrodes, J. Mater. Chem. 20 (2010) 5983–5992.
[9] G. Wang, L. Zhang, J. Zhang, A review of electrode materials for electrochemical supercapacitors, Chem. Soc. Rev. 41 (2012) 797–828.
[10] M. Sevilla, R. Mokaya, Energy storage applications of activated carbons: supercapacitors and hydrogen storage, Energy Environ. Sci. 7 (2014) 1250–1280.
[11] M.M. Samy, M.G. Mohamed, S.W. Kuo, Pyrene-functionalized tetraphenylethylene polybenzoxazine for dispersing single-walled carbon nanotubes and energy storage, Compos. Sci. Technol. 199 (2020) 108360.
[12] Z.Y. Song, D.Z. Zhu, D.F. Xue, J.J. Yan, X.L. Chai, W. Xiong, Z.W. Wang, Y.K. Lv, T.C. Cao, M.X. Liu, L.H. Gan, Nitrogen-enriched hollow porous carbon nanospheres with tailored morphology and microstructure for all-solid-state symmetric supercapacitors, ACS Appl. Energy Mater. 1 (2018) 4293–4303.
[13] J. Wei, D. Zhou, Z. Sun, Y. Deng, Y. Xia, D.A. Zhao, Controllable synthesis of rich nitrogen-doped ordered mesoporous carbon for CO_2 capture and supercapacitors, Adv. Funct. Mater. 23 (2013) 2322–2328.
[14] N.P. Wickramaratne, J. Xu, M. Wang, L. Zhu, L. Dai, M. Jaroniec, Nitrogen enriched porous carbon spheres: attractive materials for supercapacitor electrodes and CO_2 adsorption, Chem. Mater. 26 (2014) 2820–2828.
[15] S. Uppugalla, U. Male, P. Srinivasan, Design and synthesis of heteroatoms doped carbon/polyaniline hybrid material for high performance electrode in supercapacitor application, Electrochim. Acta 146 (2014) 242–248.
[16] C. Wang, L. Sun, Y. Zhou, P. Wan, X. Zhang, J. Qiu, P/N co-doped microporous carbons from H_3PO_4-doped polyaniline by in situ activation for supercapacitors, Carbon 59 (2013) 537–546.
[17] Y. Li, S. Zhang, H. Song, X. Chen, J. Zhou, S. Hong, New insight into the heteroatom-doped carbon as the electrode material for supercapacitors, Electrochim. Acta 180 (2015) 879–886.
[18] M. Sevilla, A.B. Fuertes, Direct synthesis of highly porous interconnected carbon nanosheets and their application as high-performance supercapacitors, ACS Nano 8 (2014) 5069–5078.
[19] G. Xu, H. Dou, X. Geng, J. Han, L. Chen, H. Zhu, Free standing three-dimensional nitrogen-doped carbon nanowire array for high-performance supercapacitors, Chem. Eng. J. 308 (2017) 222–228.
[20] Y.T. Liao, E.M. Matsagar, K.C.W. Wu, Metal-Organic Framework (MOF)-Derived Effective Solid Catalysts for Valorization of Lignocellulosic Biomass, ACS Sustain. Chem. Eng. 6 (2018) 13628–13643.
[21] Y.T. Liao, N.V. Chi, N. Ishiguro, A.P. Young, C.K. Tsung, K.C.W. Wu, Engineering a homogeneous alloy-oxide interface derived from metalorganic frameworks for selective oxidation of 5-hydroxymethylfurfural to 2,5-furandicarboxylic acid, Appl. Catal. B Environ. 270 (2020) 118805.
[22] S. Dutta, J. Kim, Y. Ide, J.H. Kim, M.S.A. Hossain, Y. Bando, Y. Yamauchi, K.C.W. Wu, 3D network of cellulose-based energy storage devices and related emerging applications, Mater. Horiz. 4 (2017) 522–545.
[23] Z. Deliballi, B. Kiskan, Y. Yagci, Advanced polymers from simple benzoxazines and phenols by ring-opening addition reactions, Macromolecules 53 (2020) 2354–2361.
[24] M.G. Mohamed, S.W. Kuo, Crown ether-functionalized polybenzoxazine for metal ion adsorption, Macromolecules 53 (2020) 2420–2429.
[25] K. Zhang, H. Ishida, Polymerization of an AB-type benzoxazine monomer toward different polybenzoxazine networks: when diels-alder reaction meets benzoxazine chemistry in a single-component resin, Macromolecules 52 (2019) 7386–7395.
[26] M. Arslan, B. Kiskan, Y. Yagci, Benzoxazine-based thermoset with autonomous self-healing and shape recovery, Macromolecules 51 (2018) 10095–10103.
[27] M.G. Mohamed, S.W. Kuo, Functional silica and carbon nanocomposites based on polybenzoxazines, Macromol. Chem. Phys. 220 (2019) 1800306–1800318.
[28] M.G. Mohamed, S.W. Kuo, Polybenzoxazine/Polyhedral Oligomeric Silsesquioxane (POSS) nanocomposites, Polymers 8 (2016) 225–244.
[29] W.C. Chen, S.W. Kuo, Ortho-imide and allyl groups effect on highly thermally stable polybenzoxazine/double-decker-shaped polyhedral silsesquioxane hybrids, Macromolecules 51 (2018) 9602–9612.
[30] N. Teng, S. Yang, J. Dai, S. Wang, J. Zhao, J. Zhu, X. Liu, Making benzoxazine greener and stronger: renewable resource, microwave irradiation, green solvent, and excellent thermal properties, ACS Sustain. Chem. Eng. 7 (2019) 8715–8723.
[31] C. Ma, L. Han, Z. Ma, H. Ishida, Preparation and characterization of carbon fiber reinforced polybenzoxazine and polybenzoxazole composites from the same precursor: Use of a smart, *ortho*-substituted and amide-co-imide functional matrix, Compos. Sci. Technol. 195 (2020) 108205.
[32] A.F.M. El-Mahdy, S.W. Kuo, Direct synthesis of poly(benzoxazine imide) from an *ortho*-benzoxazine: its thermal conversion to highly cross-linked polybenzoxazole and blending with poly(4-vinylphenol), Polym. Chem. 9 (2018) 1815–1826.
[33] F.S. Gungor, B. Bati, B. Kiskan, Combining naphthoxazines and benzoxazines for non-symmetric curable oxazines by one-pot synthesis, Eur. Polym. J. 121 (2019) 109352.
[34] B. Akkus, B. Kiskan, Y. Yagci, Combining polybenzoxazines and polybutadienes via simultaneous inverse and direct vulcanization for flexible and recyclable thermosets by polysulfide dynamic bonding, Polym. Chem. 10 (2019) 5743–5750.
[35] X. Zhang, M.G. Mohamed, Z. Xin, S.W. Kuo, A tetraphenylethylene-functionalized benzoxazine and copper(II) acetylacetonate form a high-performance polybenzoxazine, Polymer 201 (2020) 122552.
[36] M.G. Mohamed, S.W. Kuo, A. Mahdy, I.M. Ghayd, K.I. Aly, Bisbenzylidene cyclopentanone and cyclohexanone-functionalized polybenzoxazine nanocomposites: Synthesis, characterization, and use for corrosion protection on mild steel, Mater. Today Commun. 25 (2020) 101418.
[37] M.G. Mohamed, S.M. Ebrahium, A.S. Hammam, S.W. Kuo, K.I. Aly, Enhanced CO_2 capture in nitrogen-enriched microporous carbons derived from Polybenzoxazines containing azobenzene and carboxylic acid units, J. Polym. Res. 197 (2020) 27.

[38] A.A. Alhwaige, H. Ishida, S. Qutubuddin, Carbon aerogels with excellent CO_2 adsorption capacity synthesized from clay reinforced biobased chitosan-polybenzoxazine nanocomposites, ACS Sustain. Chem. Eng. 4 (2016) 1286–1295.
[39] R.C. Lin, M.G. Mohamed, S.W. Kuo, Benzoxazine/triphenylamine-based dendrimers prepared through facile one-pot Mannich condensations, Macromol. Rapid Commun. 38 (2017) 1700251.
[40] A. Ghosh, S. Shukla, G.S. Khosla, B. Lochab, S. Mitra, Sustainable sulfur-rich copolymer/graphene composite as lithium sulfur battery cathode with excellent electrochemical performance, Sci. Rep. 6 (2016) 25207.
[41] R.C. Lin, S.W. Kuo, Well-defined benzoxazine/triphenylamine-based hyperbranched polymers with controlled degree of branching, RSC Adv. 8 (2018) 13592–13611.
[42] S. Rimdusit, H. Ishida, Development of new class of electronic packaging materials based on ternary systems of benzoxazine, epoxy, and phenolic resins, Polymer 41 (2000) 7941–7949.
[43] K. Zhang, X. Yu, S.W. Kuo, Outstanding dielectric and thermal properties of main chain-type poly(benzoxazine-co-imide-co-siloxane)-based cross-linked networks, Polym. Chem. 10 (2019) 2387–2396.
[44] L. Wan, J. Wang, L. Xie, Y. Sun, K. Li, Nitrogen-enriched hierarchically porous carbons prepared from polybenzoxazine for high-performance supercapacitors, ACS Appl. Mater. Interface. 6 (2014) 15583–15596.
[45] L. Wan, J. Wang, Y. Sun, C. Feng, K. Li, Polybenzoxazine-based nitrogen-containing porous carbons for high-performance supercapacitor electrodes and carbon dioxide capture, RSC Adv. 5 (2015) 5331–5342.
[46] N. Amarnath, S. Shukla, B. Lochab, Harvesting the benefits of inherent reactive functionalities in fully bio-sourced isomeric benzoxazines, ACS Sustain.. Chem. Eng. 6 (2018) 15151–15161.
[47] M.G. Mohamed, R.C. Lin, J.H. Tu, F.H. Lu, J.L. Hong, K.U. Jeong, C.F. Wang, S.W. Kuo, Thermal property and aggregation-induced emission fluorophore that forms metal-ligand complexes with $Zn(ClO_4)_2$ of salicylaldehyde azine-functionalized polybenzoxazine, RSC Adv. 5 (2015) 65635–65645.
[48] M.G. Mohamed, W.C. Su, Y.C. Lin, C.F. Wang, J.K. Chen, K.U. Jeong, S.W. Kuo, Azopyridine-functionalized benzoxazine with $Zn(ClO_4)_2$ form high-performance polybenzoxazine stabilized through metal–ligand coordination, RSC Adv. 4 (2014) 50373–50385.
[49] Y. Liu, L. Cao, J. Luo, Y. Peng, Q. Ji, J. Dai, J. Zhu, X. Liu, Biobased nitrogen-and oxygen-codoped carbon materials for high-performance supercapacitor, ACS Sustain. Chem. Eng. 7 (2019) 2763–2773.
[50] Y. Wang, S. You, J. Hu, K. Zhang, Synthesis and properties of benzoxazine monomers bearing both 3-methyltetrahydrophtalimide and nitrile groups: para-para vs. ortho-ortho, Macromol. Res. 28 (2020) 74–81.
[51] X. Yu, K. Zhang, Studies on the isomeric effect of nitrile functionality on the polymerization and thermal properties of *ortho*-norbornene-based benzoxazine resins, J. Polym. Res. 27 (2020) 130.
[52] Q.L. Zhao, X.Y. Wang, C. Wu, J. Liu, H. Wang, J. Gao, Y.W. Zhang, H.B. Shu, Supercapacitive performance of hierarchical porous carbon microspheres prepared by simple one-pot method, J. Power Sources. 254 (2014) 10–17.
[53] M.G. Mohamed, M.Y. Tsai, W.C. Su, A.F.M. EL-Mahdy, C.F. Wang, C.F. Huang, L. Dai, T. Chen, S.W. Kuo, Nitrogen-doped microporous carbons derived from azobenzene and nitrile-functionalized polybenzoxazines for CO_2 uptake, Mater. Today Commun. 24 (2020) 101111.
[54] J.Y. Wu, M.G. Mohamed, S.W. Kuo, Directly synthesized nitrogen-doped microporous carbons from polybenzoxazine resins for carbon dioxide capture, Polym. Chem. 8 (2017) 5481–5489.
[55] H.E. Kissinger, Reaction kinetics in differential thermal analysis, Anal. Chem. 29 (1957) 1702–1706.
[56] M.L. Salum, D. Iguchi, C.R. Arza, L. Han, H. Ishida, P. Froimowicz, Making benzoxazines greener: design, synthesis, and polymerization of a biobased benzoxazine fulfilling two principles of green chemistry, ACS Sustain. Chem. Eng. 6 (2018) 13096–13106.
[57] D.S. Yuan, J.X. Chen, J.H. Zeng, S.X. Tan, Preparation of monodisperse carbon nanospheres for electrochemical capacitors, Electrochem. Commun. 10 (2008) 1067–1070.
[58] J. Wang, P. Zhang, L. Liu, Y. Zhang, J. Yang, Z. Zeng, S. Deng, Controllable synthesis of bifunctional porous carbon for efficient gas-mixture separation and high-performance supercapacitor, Chem. Eng. J. 348 (2018) 57–66.
[59] L.F. Chen, X.D. Zhang, H.W. Liang, M.G. Kong, Q.F. Guan, P. Chen, Z.Y. Wu, S.H. Yu, Synthesis of nitrogen-doped porous carbon nanofibers as an efficient electrode material for supercapacitors, ACS Nano 6 (2012) 7092–7102.
[60] J.D. Hulicova, M. Kodama, S. Shiraishi, H. Hatori, Z.H. Zhu, G.Q. Lu, Nitrogen-enriched nonporous carbon electrodes with extraordinary supercapacitance, Adv. Funct. Mater. 19 (2009) 1800–1809.
[61] B. Xu, H. Duan, M. Chu, G.P. Cao, Y.S. Yang, Scalable preparation of hierarchical porous activated carbon/graphene composite for high-performance supercapacitors, J. Mater. Chem. A. 1 (2013) 4565–4570.
[62] B. Xu, S.S. Hou, G.P. Cao, F. Wu, Y.S. Yang, Sustainable nitrogen-doped porous carbon with high surface areas prepared from gelatin for supercapacitors, J. Mater. Chem. 22 (2012) 19088–19093.
[63] J. Yan, T. Wei, W. Qiao, Z. Fan, L. Zhang, T. Li, Q.A. Zhao, High-performance carbon derived from polyaniline for supercapacitors, Electrochem. Commun. 12 (2010) 1279–1282.
[64] X. Hong, K.S. Hui, Z. Zeng, K.N. Hui, L. Zhang, M. Mo, M. Li, Hierarchical nitrogen-doped porous carbon with high surface area derived from endothelium Corneum Gigeriae Galli for high performance supercapacitor, Electrochim. Acta 130 (2014) 464–469.
[65] Y. Zheng, S. Li, X. Liu, P. Li, L. Sun, R. Yang, S. Wang, Z. Wu, X. Bao, W.Q. Deng, Conductive microporous covalent triazine-based framework for high-performance electrochemical capacitive energy storage, Angew. Chem., Int. Ed. 57 (2018) 7992–7996.
[66] Y. Liu, X. Hao, L. Wang, Y. Xu, J. Liu, X. Tian, B. Yao, Facile synthesis of porous carbon materials with extra high nitrogen content for supercapacitor electrodes, New. J. Chem. 43 (2019) 3713–3718.
[67] M.G. Mohamed, A.F.M. EL-Mahdy, M.M.M. Ahmed, S.W. Kuo, Direct synthesis of microporous bicarbazole-based covalent triazine frameworks for high-performance energy storage and carbon dioxide uptake, ChemPlusChem 84 (2019) 1767–1774.
[68] A.F.M. EL-Mahdy, C.H. Kuo, A. Alshehri, C. Young, Y. Yamauchi, J. Kim, S.W. Kuo, Strategic design of triphenylamine- and triphenyltriazine-based two-dimensional covalent organic frameworks for CO_2 uptake and energy storage, J. Mater. Chem. A 6 (2018) 19532–19541.
[69] M.G. Mohamed, A.F.M. EL-Mahdy, Y. Takashi, S.W. Kuo, Ultrastable conductive microporous covalent triazine frameworks based on pyrene moieties provide high-performance CO_2 uptake and supercapacitance, New J. Chem. 44 (2020) 8241–8253.
[70] Y. Li, S. Zheng, X. Liu, P. Li, L. Sun, R. Yang, S. Wang, Z. Wu, X. Bao, W.Q. Deng, Conductive microporous covalent triazine-based framework for high-performance electrochemical capacitive energy storage, Angew. Chem., Int. Ed. 57 (2018) 7992–7996.
[71] S. Dutta, A. Bhaumik, K.C.W. Wu, Hierarchically porous carbon derived from polymers and biomass: effect of interconnected pores on energy applications, Energy Environ. Sci. 7 (2014) 3574–3592.
[72] J.G. Li, P.Y. Lee, M.M.M. Ahmed, M.G. Mohamed, S.W. Kuo, Varying the hydrogen bonding strength in phenolic/PEO-b -PLA blends provides mesoporous carbons having large accessible pores suitable for energy storage, Macromol. Chem. Phys. 221 (2020) 2000040.
[73] M.G. Mohamed, W.S. Hung, A.F.M. EL-Mahdy, M.M.M. Ahmed, L. Dai, T. Chen, S.W. Kuo, High-molecular-weight PLA-b-PEO-b-PLA triblock copolymer templated large mesoporous carbons for supercapacitors and CO_2 capture, Polymers 12 (2020) 1193.
[74] A.F.M. El-Mahdy, Y.H. Hung, T.H. Mansoure, H.H. Yu, T. Chen, S.W. Kuo, A hollow microtubular triazine- and benzobisoxazole-based covalent organic framework presenting sponge-like shells that functions as a high-performance supercapacitor, Chem. Asian J. 14 (2019) 1429–1435.
[75] H. Zhang, L. Xu, G. Liu, Synthesis of benzoxazine-based N-doped mesoporous carbons as high-performance electrode materials, Appl. Sci. 10 (2020) 422.